

Oxygen-Chlorine Chemisorption Scaling for Seawater Electrolysis on Transition Metals: The Role of Redox

Robert B. Wexler and Emily A. Carter*

To clarify what controls species oxidation selectivity in seawater electrolysis, density functional theory (DFT) is used to identify chemisorption enthalpy trends and scaling relations for the simplest relevant adsorbates (O, Cl, and H) on relevant surfaces of 3d transition metals, as well as Pd and Pt, in face-centered-cubic and, if different, their ground-state crystal structures. Approximations are tested for electron exchange-correlation (XC) and van der Waals interactions to assess their ability to reproduce experimental adsorption enthalpies of H and O on Pt(111). The vdW-uncorrected generalized gradient approximation to XC of Perdew, Burke, and Ernzerhof (PBE) agrees most closely with experiments. Using DFT-PBE thereafter, it is determined that the O chemisorption enthalpy on this wide range of transition-metal surfaces is proportional to the sum of first and second atomic ionization energies, akin to a Born–Haber cycle for a redox reaction, indicating that metal redox activity controls O chemisorption strength. Then it is shown that the O and Cl chemisorption enthalpies are strongly correlated, suggesting that the transition metals considered will oxidize unselectively water and Cl^- . This strong correlation appears also for crystal reduction potentials of binary oxides and chlorides, indicating a fundamental challenge for future seawater electrode materials design.

1. Introduction

Climate change already has led to an increase in the number, duration, and intensity of wildfires, droughts, and tropical storms.^[1] Seawater CO_2 mineralization potentially could help mitigate these and other effects of climate change by reducing the amount of CO_2 in the ocean and atmosphere.^[2] To overcome the thermodynamic and kinetic barriers to carbonate precipitation in seawater CO_2 mineralization, electrolytic hydrogen production from water splitting can be used to create a locally basic environment near the cathode that stabilizes $\text{CO}_3^{2-}(\text{aq})$ and therefore facilitates its direct association with $\text{Ca}^{2+}(\text{aq})$ and $\text{Mg}^{2+}(\text{aq})$.^[3] Direct seawater electrolysis has the potential to conserve limited freshwater resources^[4] during sustainable hydrogen production and avoids the expense of desalination.^[5]

R. B. Wexler, E. A. Carter
Department of Mechanical and Aerospace Engineering and the Andlinger Center for Energy and the Environment
Princeton University
Princeton, NJ 08544-5263, USA
E-mail: eac@princeton.edu

 The ORCID identification number(s) for the author(s) of this article can be found under <https://doi.org/10.1002/adts.202200592>

DOI: 10.1002/adts.202200592

Despite the promise of electrolysis-enabled seawater CO_2 mineralization coupled with renewable hydrogen production from non-freshwater sources, state-of-the-art electrolysis anodes typically oxidize both $\text{H}_2\text{O}(\text{l})$, to the desired product $\text{O}_2(\text{g})$, and $\text{Cl}^-(\text{aq})$, to the undesired products $\text{Cl}_2(\text{g})$, and chlorine oxoacids and oxyanions.^[6] Trasatti showed long ago that the experimental overpotentials for $\text{O}_2(\text{g})$ and $\text{Cl}_2(\text{g})$ evolution are correlated for a number of oxide electrodes.^[7] Subsequently, others theoretically established linear scaling relations (linear correlations) between the O and Cl chemisorption energies for rutile (110) oxide surfaces,^[8,9] oxidized graphene,^[10] and Ni-22Cr alloys.^[11] To break this scaling and therefore suppress $\text{Cl}^-(\text{aq})$ oxidation, a few strategies have been suggested. These include sustaining the desired current with overpotentials $< 480 \text{ mV}$ ^[12] and $\text{pH} > 7.5$,^[13] using $\text{Cl}^-(\text{aq})$ -impermeable overlayers,^[14] and heteroatom substitution.^[15–20] That said, these strategies, to the best of our knowledge, have not yet produced economically

viable seawater electrolyzers. Thus, fundamental studies of seawater electrolysis—starting with understanding the simplest relevant adsorbates on the surfaces of transition-metal elements (whose compounds comprise an important direction for anode design)—are needed.

In this work, we utilize (and benchmark) density functional theory (DFT) calculations and ordinary least-squares linear regression to understand O, Cl, and H chemisorption enthalpy trends and scaling on 3d transition metals, Pd, and Pt in the face-centered cubic (fcc) and their ground-state (e.g., hexagonal close-packed Sc) crystal structures. We then discuss the consequences of our linear model for the O chemisorption enthalpy, which is based on the sum of the first and second atomic ionization energies, with an emphasis on the universality of metal redox activity as a catalysis descriptor.^[21] Lastly, we discuss the implications of O–Cl chemisorption scaling for the design of $\text{O}_2(\text{g})$ -selective seawater electrolysis anodes.

2. Experimental Section

2.1. Quantum Mechanics Calculations

DFT calculations of H, O, and Cl adsorption enthalpies were performed using the Vienna Ab initio Simulation Package

(VASP) version 5.4.4.^[22,23] For the exchange-correlation (XC) functional, the Perdew–Burke–Ernzerhof (PBE) generalized gradient approximation (GGA)^[24] and the strongly constrained and appropriately normed (SCAN) meta-GGA were considered.^[25] To include van der Waals (vdW) interactions, which often are necessary for accurately simulating chemisorption at finite coverage, the DFT-D2^[26] and DFT-D3 (without^[27] and with^[28] Becke–Johnson [BJ] damping)^[29–31] corrections for PBE and the rVV10 functional for SCAN were considered.^[32] The PBE PAW data sets suggested by the Materials Project^[33] for Sc ($3s^2 3p^6 4s^2 3d^1$), Ti ($3p^6 4s^2 3d^2$), V ($3s^2 3p^6 4s^2 3d^3$), Cr ($3p^6 4s^1 3d^5$), Mn ($3p^6 4s^2 3d^5$), Fe ($3p^6 4s^2 3d^6$), Co ($4s^2 3d^7$), Ni ($3p^6 4s^2 3d^8$), Cu ($3p^6 4s^1 3d^{10}$), Zn ($4s^2 3d^{10}$), Pd ($5s^0 4d^{10}$), Pt ($6s^1 5d^9$), H ($1s^1$), O ($2s^2 2p^4$), and Cl ($3s^2 3p^5$) were employed, where the electronic configurations listed here represent those electronic wavefunctions that are optimized self-consistently. These outer-core/valence-electron wave functions were expanded in a plane-wave basis with a kinetic energy cutoff of 770 eV, as this converges the total energies of all systems considered, set by $O_2(g)$, to within 1 meV per atom (see Figure S1, Supporting Information for the convergence test). Methfessel–Paxton first-order electronic smearing^[34] of 0.2 eV to the band occupations near the Fermi energy to improve self-consistent field convergence was applied. For the one-atom primitive rhombohedral cell of face-centered cubic (fcc) Pt (PBE-calculated lattice constant $a_{\text{Pt}} = 2.81$ Å and angle = 60°), a $25 \times 25 \times 25$, Γ -point-centered k -point grid (see Figure S2, Supporting Information for the convergence test) was used. For other metals, the number of k -points per lattice constant of Pt (25) was scaled by a_{Pt}/a , where a is the lattice constant of the other metal. The Accurate “precision”-mode in VASP was adopted to prevent fast Fourier transform wraparound errors and to represent more accurately the pseudo-orbitals. The projection operators in real space were calculated using the automatic optimization method in VASP.

Spin-polarized DFT calculations were carried out with a ferromagnetic (FM) initial spin alignment for Sc, Ti, V, Co, Ni, Cu, Zn, Pd, and Pt, and both FM and three types of antiferromagnetic (AFM) initial spin alignments for Cr, Mn, and Fe (see Figures S3–S5, and Table S1 in the Supporting Information). An initial FM state was chosen for paramagnetic (Sc, Ti, V, Pd, and Pt) and diamagnetic (Cu and Zn) elements so as not to prohibit open-shell configurations produced by surface formation and adsorption. Self-consistent-field convergence was judged to have been attained when the energy change between electronic minimization steps was $\leq 1 \times 10^{-5}$ eV per cell. For ionic relaxation, the quasi-Newton algorithm was used first, switching to the conjugate-gradient algorithm for problematic structures and ending either algorithm when all the atomic force magnitudes were $\leq 1 \times 10^{-2}$ eV Å⁻¹. For surface calculations, dipole corrections were applied to the energy and potential based on the implementation of Neugebauer and Scheffler.^[35] VASP zone-center (Γ -point) vibrational frequencies were computed by diagonalizing Hessians constructed from finite central differences of atomic forces induced by small atomic displacements. Specifically, adsorbates and metal atoms were displaced in the topmost surface layer by ± 0.015 Å along each of the Cartesian directions,

Table 1. Ground-state crystal structures, and minimum-surface-energy and maximum-area-fraction facets of 3d transition metals, Pd, and Pt.

Element	Crystal structure	Facets	
		Min. surface energy	Max. area fraction
Sc	hcp	(10 $\bar{1}$ 0)	(10 $\bar{1}$ 1)
Ti	hcp	(11 $\bar{2}$ 0)	(10 $\bar{1}$ 1)
V	bcc	(100)	(110)
Cr	bcc		(110)
Fe	bcc		(110)
Co	hcp	(0001)	(10 $\bar{1}$ 1) and (10 $\bar{1}$ 0)
Ni	fcc		(111)
Cu	fcc		(111)
Zn	hcp	(0001)	(10 $\bar{1}$ 0)
Pd	fcc		(111)
Pt	fcc		(111)

with a global break condition for the total (free) energy change of 1×10^{-8} eV per cell.

2.2. Systems

O, Cl, and H chemisorption was considered on the relatively abundant 3d transition metals (Sc, Ti, V, Cr, Mn, Fe, Co, Ni, Cu, and Zn), Pd, and technologically relevant Pt,^[36] whose bulk ground-state crystal structures are listed in **Table 1**. These structures include hexagonal close-packed (hcp) for Sc, Ti, Co, and Zn; body-centered cubic (bcc) for V, Cr, and Fe; and face-centered cubic (fcc) for Cu, Ni, Pd, and Pt. Sc, Ti, V, Cr, Mn, Fe, Co, and Zn were considered in the fcc crystal structure to isolate structure-independent trends for and scaling of O, Cl, and H chemisorption enthalpies. The ground-state I43m crystal structure of bulk Mn was not considered due to the great number of energetically accessible magnetic structures of its surfaces without and with adsorbates.

For fcc metals, O, Cl, and H chemisorption at fcc threefold hollows (no metal atom right below the adsite) on the (111) facet was examined. Table 1 lists the surfaces which were investigated for metals in their ground-state crystal structures. Only the minimum-surface-energy and maximum-area-fraction of the Wulff shape, low-Miller-index [$\max\{h, k, l\} \leq 1$ for non-hexagonal lattices and $\max\{h, k, i, l\} \leq 2$ for hexagonal lattices] facets in Crystalium were selected.^[37] 20-atom supercells containing five atomic layers were employed to represent the surfaces. The atoms in the two topmost layers of the five-layer, 20-atom supercell were relaxed, while the atoms in the three bottommost layers of the supercell were fixed at their bulk atomic positions to set the correct boundary condition of a semi-infinite bulk crystal. For these selected facets, pymatgen’s AdsorbateSiteFinder^[38] was used to construct all possible symmetry-distinct O, Cl, and H chemisorption geometries. The H adsorption enthalpy was calculated because it has the most experimental values for

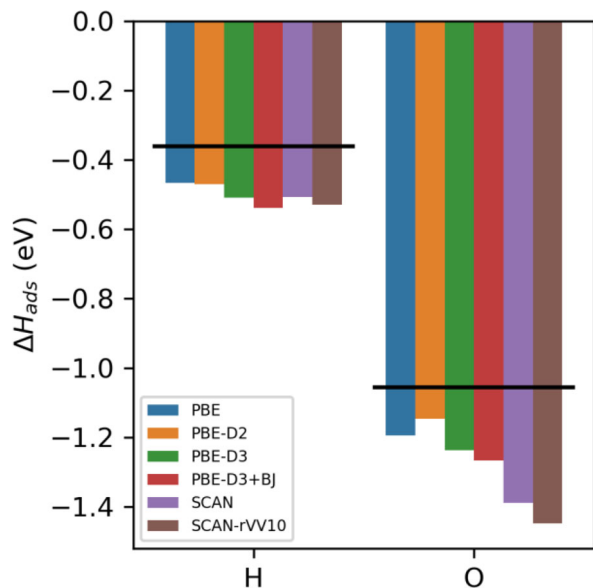


Figure 1. Exchange-correlation functional and van der Waals correction benchmarking of H ($\theta = 1/4$) and O ($\theta = 1/9$) adsorption enthalpies $\Delta H_{\text{ads}} = \Delta E_{\text{ads}} + \Delta ZPE_{\text{ads}}$ on the (111) surface of Pt. Black lines are experimental adsorption energies extrapolated to 0 K.^[40]

benchmarking. Finally, ordinary least-squares linear regression in scikit-learn^[39] was used for supervised learning of the O chemisorption enthalpy.

3. Results

3.1. XC-vdW Benchmarking

Prior to analyzing adsorption enthalpy trends and scaling relations, we first had to identify an appropriate level of theory, which here we define as the XC-functional/vdW-correction combination that reproduces most accurately experimental adsorption energies, i.e., experimental adsorption enthalpies extrapolated to 0 K, which include zero-point energy changes (ΔZPE s). Throughout, we refer to these as “experiment.” Of the transition metals we considered, fcc Pt(111) is the best choice for such benchmarking because experimental H and O adsorption enthalpies are available.^[40] While we focus on atomic (H and O) adsorption at the stronger-binding fcc hollow site, we also consider their chemisorption at the weaker-binding hcp threefold hollow sites (metal atom right below site) in Figure S6 (Supporting Information). Specifically, we define atomic (A) adsorption as $* + 1/2 A_2(g) \rightarrow A^*$, where $*$ is an unoccupied surface site and A^* is an atomic adsorbate. For XC-vdW benchmarking of H and O adsorption at the fcc hollow site on fcc Pt(111), we simulate coverages (θ) of 1/4 and 1/9 ML, respectively, as these correspond to the experimental conditions presented in ref. [40].

Figure 1 shows how the 0-K adsorption enthalpies ΔH_{ads} of H ($\theta = 1/4$) and O ($\theta = 1/9$) on Pt(111) depend on the choice of the XC functional and vdW correction from the following set of combinations: PBE (blue bars), PBE-D2 (orange), PBE-D3 (green), PBE-D3+BJ (red), SCAN (purple), and SCAN-rVV10 (brown). First, we find that all XC-vdW approximations

considered overbind these two adsorbates compared to experiments (black lines). Moreover, we observe that vdW corrections strengthen adsorption, except for O with PBE-D2 (PBE-D2 = -0.82 eV > PBE = -0.85 eV), and hence tend to exacerbate this overbinding. Overall, PBE best agrees with experiments for H ($|\text{error}| = 0.11$ eV) and is only slightly worse than PBE-D2 for O (PBE-D2 $|\text{error}| = 0.12$ eV < PBE $|\text{error}| = 0.17$ eV). Since the difference between the PBE-D2 and PBE $|\text{error}|$ (0.05 eV) is less than typical DFT errors in reaction energies (± 0.1 eV), we opt for the non-empirical, vdW-uncorrected PBE throughout. Note that because PBE overbinds $O_2(g)$, i.e., the PBE bond dissociation enthalpy (E_b) = 6.06 eV > experimental $E_b = 5.12$ eV, its agreement with experiments is likely due to overbinding O^* also and consequently fortuitous error cancellation. We note that with such small adsorbates, the conclusion that vdW corrections are not necessary is not particularly surprising but was important to ascertain at the beginning.

3.2. Chemisorption Trends for FCC Transition Metals

Having identified vdW-uncorrected DFT-PBE as an appropriate level of theory, we now analyze adsorption enthalpy trends and scaling relations for the surfaces of 3d transition metals, Pd, and Pt. We begin by studying these metals in the fcc crystal structure (see **Figure 2**) as this controls for the bulk, surface, and adsorption site structure, while allowing variations in electronic structure and stability, since fcc is not the ground-state (gs) crystal structure for Sc ($E_{\text{fcc}} - E_{\text{gs}} = 0.05$ eV per atom), Ti (0.06 eV per atom), V (0.24 eV per atom), Cr (0.40 eV per atom), Mn (0.08 eV per atom), Fe (0.15 eV per atom), Co (0.02 eV per atom), and Zn (0.02 eV per atom). Additionally, experimental chemisorption enthalpies are available for O ($\theta = 1/4$) and H ($\theta = 1/4$) chemisorption on fcc Ni(111), H ($\theta = 1/4$) chemisorption on fcc Pd(111), and O ($\theta = 1/9$) and H ($\theta = 1/4$) chemisorption on Pt (vide supra).^[40] We focused on simple adsorbates (O, Cl, and H) to build fundamental understanding; considering HO, H_2O , and Cl oxoacid and oxyanion adsorption will be the focus of future work.

Figure 2a displays and **Table 2** lists the periodic trends in the chemisorption enthalpies of O (blue circles), Cl (orange triangles), and H (green squares) at $\theta = 1/4$ for transition metals in the fcc structure, with elements listed by ascending atomic number (see Figure S7, Supporting Information for optimized geometries). Firstly, we obtain good agreement between theory and experiment (black outlined circles and squares). Note that we are always comparing—for the cases where there is experimental data—enthalpies at the same coverage. Furthermore, consistent with known trends, the transition metals become more unreactive (chemisorption enthalpies decrease) moving from left to right (i.e., Sc to Zn) and from top to bottom (i.e., Ni to Pt).^[41] We find that this general, monotonic trend for the O chemisorption enthalpy ΔH_O can be explained quantitatively ($R^2 = 0.97$ and mean absolute error [MAE] = 0.26 eV) by the sum of the first and second atomic ionization energies $\sum E_i$ of the metal, as shown in **Figure 2b**.

This simple, linear model for ΔH_O can be thought of as a four-step Born–Haber cycle for purely ionic bond formation (see **Figure 3**). In Step 1 (blue), the $O_2(g)$ bond dissociates, increasing the energy of the system (surface + gas) by E_b . In Step 2

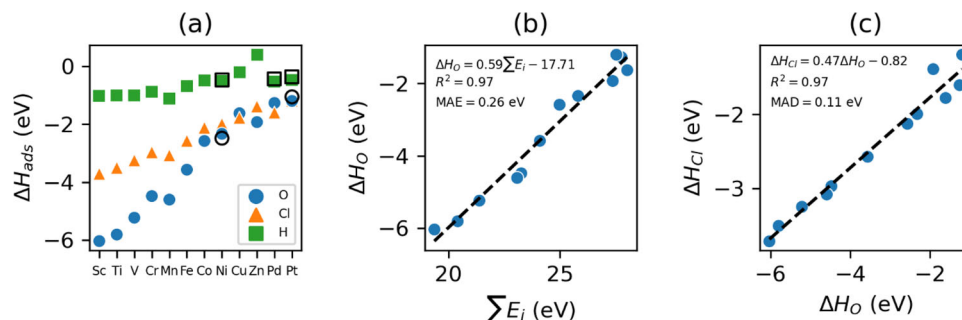


Figure 2. O, Cl, and H (all $\theta = 1/4$) chemisorption at fcc threefold-hollow sites on *isostructural* (111) surfaces of 3d transition metals, Pd, and Pt in the fcc crystal structure. a) Trends in O (blue circles), Cl (orange triangles), and H (green squares) chemisorption enthalpies $\Delta H_{\text{ads}} = \Delta E_{\text{ads}} + \Delta ZPE_{\text{ads}}$. Black outlined circles and squares are experimental O ($\theta = 1/4$ for Ni and $\theta = 1/9$ for Pt) and H ($\theta = 1/4$ for Ni, Pd, and Pt) chemisorption enthalpies, respectively.^[40] Note that the difference between the ΔH_{O} for Pt at $\theta = 1/9$ and $\theta = 1/4$ is less than 0.01 eV. b) Relationship between ΔH_{O} and the sum of the first and second metal atomic ionization energies ($\sum E_i$). The dashed black line is an ordinary least-squares linear-regression model and MAE is the mean absolute error. c) O and Cl chemisorption enthalpy (ΔH_{O} and ΔH_{Cl} , respectively) scaling. MAD is the mean absolute deviation.

Table 2. Adsorption energies (ΔE_{ads}), zero-point energies (ΔZPE_{ads}), and enthalpies (ΔH_{ads}) in eV for O, Cl, and H (all $\theta = 1/4$) chemisorption at fcc threefold-hollow sites on *isostructural* (111) surfaces of 3d transition metals, Pd, and Pt in the fcc crystal structure.

Element	ΔE_{ads}			ΔZPE_{ads}			ΔH_{ads}		
	O	Cl	H	O	Cl	H	O	Cl	H
Sc	-6.08	-3.72	-1.05	0.05	0.02	0.03	-6.03	-3.71	-1.02
Ti	-5.87	-3.55	-1.06	0.07	0.05	0.05	-5.80	-3.50	-1.01
V	-5.28	-3.28	-1.07	0.06	0.03	0.06	-5.22	-3.25	-1.00
Cr	-4.52	-2.99	-0.94	0.04	0.02	0.06	-4.48	-2.97	-0.89
Mn	-4.63	-3.09	-1.16	0.03	0.01	0.04	-4.60	-3.07	-1.12
Fe	-3.64	-2.61	-0.74	0.07	0.04	0.06	-3.57	-2.57	-0.69
Co	-2.60	-2.14	-0.54	0.02	0.01	0.04	-2.58	-2.12	-0.50
Ni	-2.37	-2.01	-0.55	0.04	0.02	0.04	-2.33	-1.99	-0.51
Cu	-1.66	-1.79	-0.23	0.04	0.01	0.03	-1.62	-1.78	-0.20
Zn	-1.95	-1.39	0.41	0.02	0.01	-0.01	-1.93	-1.39	0.40
Pd	-1.30	-1.62	-0.55	0.03	0.02	0.02	-1.27	-1.60	-0.53
Pt	-1.22	-1.20	-0.47	0.03	0.01	0.00	-1.20	-1.19	-0.47

(orange), metal atoms (M) at the unoccupied surface site are oxidized (M^{q+}), increasing further the energy of the system by $\int E_i(q) dq$, where $E_i(q)$ is the atomic ionization energy as a function of the charge q transferred during oxidation. In Step 3 (green), to charge-balance the metal oxidation, O(g) is reduced to O^{q-} (g), which decreases the system energy by $\int E_a(q) dq$, where E_a is the atomic electron affinity of O(g), defined as a negative number. Finally, in Step 4 (red), M^{q+} electrostatically attracts O^{q-} (g), decreasing the system energy by kq^2/d , where k is the Coulomb constant and d is the equilibrium distance between M^{q+} and O^{q-} after adsorption.

By combining the energies of these steps, we arrive at an expression for the change in the enthalpy of the system upon O chemisorption (purple), assuming purely ionic bonding, i.e.,

$$\Delta H_{\text{O}} = E_b/2 + q (\sum E_i + \sum E_a) / 2 - kq^2/d = m \sum E_i + b \quad (1)$$

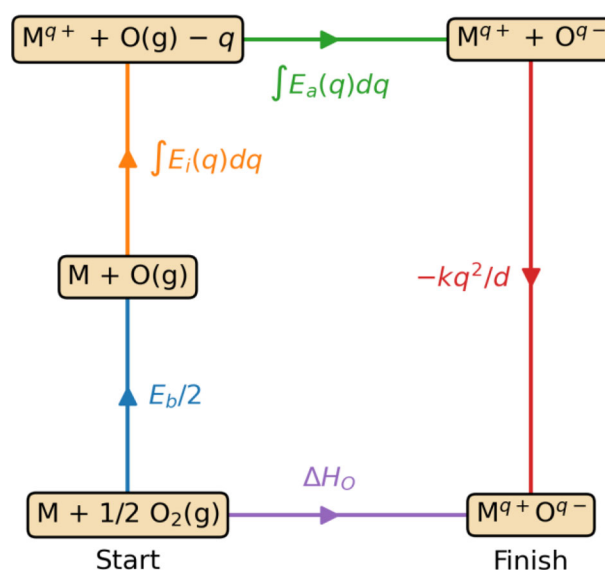


Figure 3. Four-step Born-Haber cycle for ΔH_{O} .

where E_b and $\sum E_a$ are O-derived constants, E_i , q , and d depend on the metal atom, m is the slope, and b is the intercept. The latter two quantities are determined from a least-squares fit and then those are used to derive the other unknown physical constants as follows. Note that the factor of 1/2 in the second term of Equation (1) converts $\sum E_i$ and $\sum E_a$ to potentials due to the nominal transfer of two electrons from M to O. Therefore, the slope of ΔH_{O} with respect to $\sum E_i$ ($m = q/2 = 0.59$ e) can be understood physically as half the number of electrons donated by M to O(g) upon O chemisorption ($q \approx 1.18$ e is the average number of electrons transferred, according to the linear fit). This interpretation is supported by the fact that q is in good agreement with the O^* Bader charges, which range from 1.37 e on Sc to 0.77 e on Pt. On the other hand, b is given by

$$b = E_b/2 + q \sum E_a/2 - kq^2/d = -17.71 \text{ eV} \quad (2)$$

Using $E_b = 5.12$ eV (at 0 K),^[42] $q = 1.18$ e, $\sum E_a = 1^{\text{st}} E_a + 2^{\text{nd}} E_a = -1.46$ eV + 7.71 eV = 6.25 eV (we obtain the experimental

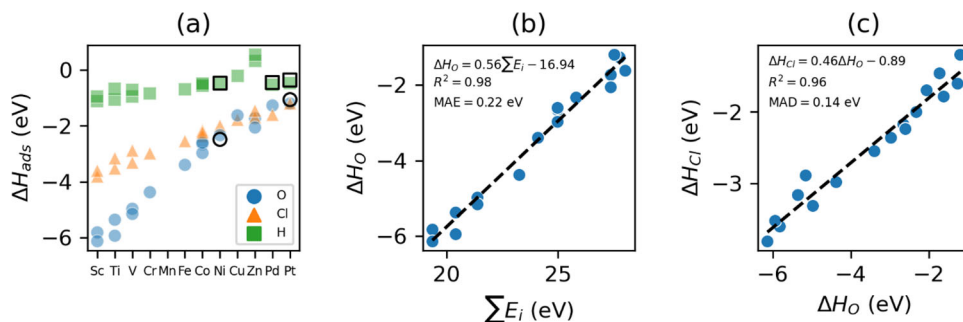


Figure 4. O, Cl, and H (all $\theta = 1/4$) chemisorption at the minimum-energy sites on selected surfaces of 3d transition metals, Pd, and Pt in their ground-state bulk crystal structures. a) Trends in O (blue circles), Cl (orange triangles), and H (green squares) adsorption enthalpies $\Delta H_{\text{ads}} = \Delta E_{\text{ads}} + \Delta ZPE_{\text{ads}}$ (see Table 3). Black outlined circles and squares are experimental O and H adsorption enthalpies, respectively.^[40] b) Relationship between ΔH_{O} and ΣE_i . The dashed black line is an ordinary least-squares linear regression model. c) ΔH_{O} and ΔH_{Cl} scaling.

1st E_a of O from ref. [42] and the semiempirical 2nd E_a of O from ref. [43]), and $k = 14.3996 \text{ eV } \text{\AA} \text{ e}^{-2}$, we solve Equation (2) for d and obtain 0.84 \AA ; this is consistent with the distances between the metal surface plane (containing the fcc threefold-hollow site) and O^* , which range from 0.83 \AA on Zn to 1.18 \AA on Pt. Interestingly, this simple ionic model yields consistent charge transfer and geometries despite the chemisorption bond actually being a mixture of covalent and ionic character.

Lastly, Figure 2c displays the scaling relationship between O and Cl chemisorption, ΔH_{O} and ΔH_{Cl} , respectively. The slope = 0.47 can be understood in one of two ways. Abild-Pedersen et al. first showed that, e.g., for CH_x ($x = 0, 1, 2,$ and 3) adsorption on a range of transition-metal surfaces, the slope only depends on the difference between the valency or bond-order (BO) of the adsorbates.^[44] Therefore, if Cl and O form a single and double bond, respectively, with the surface, then the slope $\approx \text{BO}(\text{Cl}^*)/\text{BO}(\text{O}^*) = 1/2$. Alternatively, one can interpret the slope as the difference between the oxidizing capacity of the adsorbates, i.e., the number of electrons in the oxidation of the metal to complete the octet of the adsorbate (N_e). Since the N_e of Cl and O are 1 and 2 electrons, respectively, the slope $\approx N_e(\text{Cl})/N_e(\text{O}) = 1/2$. Ultimately, this strong O–Cl scaling, with an $R^2 = 0.97$ and mean absolute deviation (MAD) = 0.11 eV, indicates that the electronic-structure and stability variations in the isostructural fcc transition metals we considered do not offer opportunities for selective seawater oxidation.

4. Chemisorption Trends for Stable Transition Metals

Despite the utility of exploring structure-independent trends, a more practical constraint is transition-metal stability. With this in mind, we now control for the stability of their bulk phases (ground-state crystal structures), surfaces (minimum-surface-energy and maximum-area-fraction facets), and adsorbates (minimum-energy chemisorption sites). Figure 4a presents and Table 3 lists the same chemisorption trends at $\theta = 1/4$ and has the same axes, colors, and Ni, Cu, Pd, and Pt data (because their ground-state crystal structure is fcc) as Figure 2a (see Figure S8, Supporting Information for optimized geometries). Note that there are two data points each for Sc (two facets), Ti (two facets), V (two facets), and Zn (two facets), and three data points

for Co (three facets, see Table 1). As the qualitative trends in adsorption enthalpies for these ground-state structures are quite similar to those of the fcc-only adsorption enthalpies (Figure 2), the chemisorption trends and scaling for stable transition-metal phases can be attributed primarily to variations in their electronic structures, with much weaker dependence on their bulk, surface, and adsorption structures.

The linear model for ΔH_{O} in Figure 4b shows that the trends again can be explained by ΣE_i , with an $R^2 = 0.98$ and MAE = 0.22 eV. Interestingly, the adsorbate coordination number (see Table 3), which ranges from two to five (see Figure S9, Supporting Information for the fivefold-coordinated O^* structures), is not needed to explain the ΔH_{O} trends, further implying that redox activity (i.e., ionic bonding) dominates ΔH_{O} .^[21] While the slope = 0.56 ($q \approx 1.12 \text{ e}$) is in good agreement with that for the fcc transition-metal (111) surfaces, the intercepts in Figures 2b and 4b, i.e., -17.71 and -16.94 eV , respectively, differ by 0.77 eV. This could be explained by small differences in equilibrium $\text{M}^{\delta+}\text{--O}^{\delta-}$ separation and/or differences in work function between the surfaces of transition metals in the fcc and their ground-state crystal structures, which are not captured by atomic ionization energies. Finally, Figure 4c demonstrates a robust O–Cl chemisorption scaling relationship ($R^2 = 0.96$ and MAD = 0.14 eV), with a slope = 0.46 and intercept = -0.89 eV , which is in good agreement with that for the fcc transition-metal (111) surfaces. This agreement indicates that O–Cl scaling is independent of the metal's bulk, surface, and minimum-energy adsorption site structure and therefore is controlled essentially entirely by the oxidizability of the metal atoms that bind the adsorbate.

5. Discussion

First, let us examine the relationship between ΔH_{O} and the electronic structure of transition metals. The most widely used method to establish such a relationship is the d-band model,^[45–49] which shows that the position of the d-band center relative to the Fermi energy controls ΔH_{O} . Our results indicate, however, that E_i also can be utilized successfully to model ΔH_{O} for adsorption on the 3d transition metals, Pd, and Pt. Zha et al. showed that E_i models also can predict the ΔE_{O} ($\approx \Delta H_{\text{O}}$) of more complex systems, such as oxides (e.g., doped rutiles, perovskites, and

Table 3. Minimum adsorption energies (ΔE_{ads}), zero-point energies (ΔZPE_{ads}), and enthalpies (ΔH_{ads}) in eV for O, Cl, and H (all $\theta = 1/4$) chemisorption at surface sites with different coordination numbers (CNs) on different facets of the 3d transition metals (except Mn), Pd, and Pt in their ground-state crystal structures (see Table S2 and Figure S10, Supporting Information for non-minimum chemisorption energies and optimized geometries, respectively).

Element	Structure	Facet	CN			ΔE_{ads}			ΔZPE_{ads}			ΔH_{ads}		
			O	Cl	H	O	Cl	H	O	Cl	H	O	Cl	H
Sc	hcp	(10 $\bar{1}$ 0)	3	2	3	-5.85	-3.62	-0.98	0.03	0.01	0.03	-5.82	-3.61	-0.95
		(10 $\bar{1}$ 1)	3	3	3	-6.16	-3.83	-1.15	0.03	0.01	0.03	-6.13	-3.81	-1.12
Ti	hcp	(11 $\bar{2}$ 0)	3	2	4	-5.40	-3.16	-0.72	0.04	0.00	0.04	-5.36	-3.16	-0.68
		(10 $\bar{1}$ 1)	5	3	3	-5.98	-3.55	-1.10	0.04	0.03	0.04	-5.94	-3.53	-1.06
V	bcc	(100)	5	2	5	-5.15	-2.85	-0.70	0.00	-0.03	-0.01	-5.15	-2.88	-0.71
		(110)	3	3	3	-5.02	-3.34	-1.00	0.05	0.02	0.05	-4.97	-3.32	-0.95
Cr	bcc	(110)	3	3	3	-4.42	-3.01	-0.87	0.04	0.02	0.04	-4.38	-2.98	-0.83
Fe	bcc	(110)	3	4	3	-3.44	-2.57	-0.73	0.04	0.02	0.04	-3.40	-2.54	-0.69
Co	hcp	(0001)	3	3	3	-2.69	-2.18	-0.55	0.04	0.01	0.04	-2.65	-2.17	-0.52
		(10 $\bar{1}$ 1)	4	3	3	-3.01	-2.38	-0.60	0.04	0.03	0.05	-2.97	-2.36	-0.55
		(10 $\bar{1}$ 0)	3	2	3	-2.64	-2.24	-0.52	0.04	0.01	0.04	-2.60	-2.23	-0.48
Ni	fcc	(111)	3	3	3	-2.37	-2.01	-0.55	0.04	0.02	0.04	-2.33	-1.99	-0.51
Cu	fcc	(111)	3	3	3	-1.66	-1.79	-0.23	0.04	0.01	0.03	-1.62	-1.78	-0.20
Zn	hcp	(0001)	3	2	3	-1.76	-1.46	0.57	0.03	0.01	-0.01	-1.72	-1.45	0.56
		(10 $\bar{1}$ 0)	3	2	2	-2.09	-1.70	0.32	0.04	0.01	0.01	-2.06	-1.69	0.33
Pd	fcc	(111)	3	3	3	-1.30	-1.62	-0.55	0.03	0.02	0.02	-1.27	-1.60	-0.53
Pt	fcc	(111)	3	3	3	-1.22	-1.20	-0.47	0.03	0.01	0.00	-1.20	-1.19	-0.47

Table 4. O–Cl chemisorption scaling on metal and metal-oxide surfaces. m and β are the slope and intercept, respectively, of the linear scaling relations, $\Delta E_{\text{Cl}} = m\Delta E_{\text{O}} + \beta$.

Materials	m	β [eV]	Reference
fcc 3d transition metals, Pd, and Pt	0.47	-0.82	This work
3d transition metals, Pd, and Pt in their ground-state bulk crystal structures	0.46	-0.89	This work
Ni-22Cr alloys with solute elements Co, Cu, Fe, Mn, Mo, Ru, and W	0.51	-0.69	[11]
Rutile IrO ₂ , RuO ₂ , PtO ₂ , and TiO ₂	0.59	-2.26	[8]
Rutile IrO ₂ , RuO ₂ , PtO ₂ , TiO ₂ , VO ₂ , SnO ₂ , and RhO ₂	0.34	-1.62	[9]

spinel), single-site alloys and catalysts, and cation-exchanged zeolites.^[50] Such models benefit from the fact that curated E_i measurements are available for most elements,^[51] unlike d-band centers/edges.

For further context, we consider the generality of O–Cl scaling. The scaling relations between O and Cl adsorption on the fcc (see Figure 2c) and stable (see Figure 4c) transition metals are approximately the same (see Table 4). This indicates that O–Cl scaling on 3d transition metals, Pd, and Pt has a relatively weak dependence on bulk stability and crystal structure (bulk and surface). These scaling relations also are very similar to those on Ni-22Cr alloys,^[11] suggesting that O–Cl scaling on transition-metal alloys weakly depends on composition. Linear scaling relations between ΔE_{Cl} and ΔE_{O} also have been established theoretically for metal coordinatively unsaturated sites on rutile oxide (110)

surfaces,^[8,9] with comparable slopes (0.34–0.59 for rutile oxides vs 0.46–0.51 for metals and metal alloys) but different intercepts. Comparable slopes signify that O–Cl scaling is a general property of both metals and their oxides.

We hypothesize that the different intercepts (β) for rutile oxides (–2.26 to –1.62 eV, mean intercept $\beta^{\text{oxide}} = -1.94$ eV) and metals and metal alloys (–0.89 to –0.69 eV, $\beta^{\text{metal}} = -0.80$ eV) comes from the difference between the work functions (W) of metals and their oxides. To establish the relationship between β and W differences, consider an approximate form of the O–Cl scaling

$$\Delta E_{\text{Cl}} = 0.5\Delta E_{\text{O}} + \beta \quad (3)$$

where we set the slope = 0.5. For a given, fixed ΔE_{O} , we can write

$$\beta^{\text{metal}} - \beta^{\text{oxide}} = \Delta E_{\text{Cl}}^{\text{metal}} - \Delta E_{\text{Cl}}^{\text{oxide}} = -0.80 + 1.94 \text{ eV} = 1.14 \text{ eV} \quad (4)$$

Since $-W$ is the electrostatic potential energy of an electron at the surface and Cl[–] has the same charge as an electron, we propose that

$$\Delta E_{\text{Cl}}^{\text{metal}} - \Delta E_{\text{Cl}}^{\text{oxide}} \approx \overline{W^{\text{oxide}} - W^{\text{metal}}} \quad (5)$$

Table S3 (Supporting Information) shows that, for the metals (Ti, Mo, Cu, Ni, W, V, Cr, Ta, and Co) and the binary oxides comprised of their corresponding metal cations with lowest oxidation state $\geq 2+$ (TiO, MoO₂, CuO, NiO, W₁₈O₄₉, V₂O₃, Cr₂O₃, Ta₂O₅,

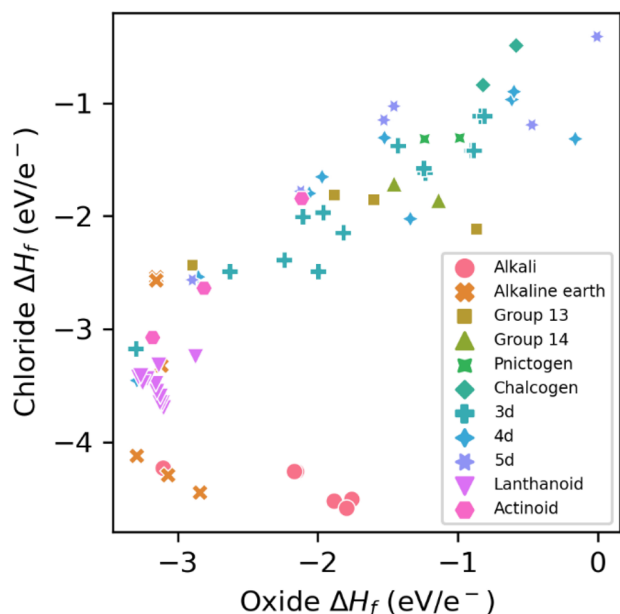


Figure 5. Correlation between experimental binary oxide and chloride crystal reduction potentials $V_r[M^{n+} \rightarrow M^0] \cong \Delta H_f/nF$, where n is the oxidation state of the metal in the binary oxide $MO_{n/2}$ or chloride MCl_n , ΔH_f is the binary formation enthalpy, and F is the Faraday constant (we are neglecting entropic contributions to the free energy, which should be small at room temperature for solid–solid transformations). If crystal reduction produces M^0 , V_r is the formation enthalpy per electron. For example, consider $V_r[Ca^{2+} \rightarrow Ca^0]$, where $M = Ca$, $n = 2$, $MO_{n/2} = CaO$. Since the experimental $\Delta H_f[CaO] = -6.58$ eV, $V_r[Ca^{2+} \rightarrow Ca^0] = -3.29$ V.

and CoO) considered in ref. [52], the mean difference between their work functions is 1.05 eV, which is in good agreement with $\beta^{\text{metal}} - \beta^{\text{oxide}} = 1.14$ eV.

Since this strong correlation appears to be a more general trend, we next analyze the scaling in the experimental crystal reduction potentials^[21] (i.e., approximately the formation enthalpy per electron at 298 K) of bulk binary oxides (V_o) and chlorides (V_{Cl}). **Figure 5** demonstrates strong scaling for all but the alkali metals (red circles)—their chlorides are more stable than their oxides because these metals can be 1+ but not 2+—and alkaline earth metals (orange crosses) Ca, Sr, and Ba. Therefore, there do not seem to be any binary, solid-state inorganic materials that selectively react with O. Since $\Delta H_{Cl} \propto \Delta H_o$ (i.e., *O and Cl chemisorption scale*) and $V_{Cl} \propto V_o$ (i.e., *oxide and chloride formation scale*) for surface and bulk phases, respectively, and $\Delta H_o \propto \sum E_i$ (*redox controls O chemisorption*), we hypothesize that the key to selective seawater electrolysis is the design of anodes with materials that easily undergo two- but not one-electron reduction (not a trivial requirement). Opportunities for designing redox-selective anodes include doping^[15–19] and exploring superbinary oxides (e.g., pyrochlores^[20]) in addition to buffer solutions^[12] and impermeable overlayers.^[14] As a final point, we hypothesize that the E_i model's accuracy, in conjunction with our crystal-reduction potential model for oxygen vacancy formation in oxide perovskites,^[21] suggests a much more predictive and universal relationship between redox activity and oxidation reactivity than may have been appreciated previously.

6. Conclusions

As had been found for select binary materials previously, we demonstrated that O and Cl chemisorption enthalpies are strongly correlated for a diverse array of pure transition metals as well. This strong correlation appears to be a more general trend, as it also appears for oxygen and chlorine evolution from the decomposition of their binary oxides and chlorides into the standard states of the species comprising them (the reverse—formation—reaction was discussed above and the correlation holds in both directions). We thus highlight the importance of fundamental studies related to seawater electrolysis—starting with the simplest adsorbates on the surfaces of transition-metal elements—but further motivate the need for future research in redox-selective anode design. Understanding, e.g., why some superbinary oxides, like $Pb_2Ru_2O_{7-x}$ pyrochlores, offer opportunities for selective seawater oxidation and how to control that selectivity are among areas for future investigation.

Supporting Information

Supporting Information is available from the Wiley Online Library or from the author.

Acknowledgements

This work was conducted within the Computational Chemical Science Center: Chemistry in Solution and at Interfaces at Princeton University, supported as part of the Computational Chemical Sciences Program funded by the U.S. Department of Energy (DoE), Office of Science, Basic Energy Sciences, under Award no. DE-SC0019394. The authors thank the National Energy Research Scientific Computing Center for computing resources. They also acknowledge the use of TIGRESS High Performance Computer Center at Princeton University.

Conflict of Interest

The authors declare no conflict of interest.

Data Availability Statement

The data that support the findings of this study are openly available in NOMAD at <https://doi.org/10.17172/NOMAD/2022.08.14-1>, reference number 0.

Keywords

chemisorption, chlorine evolution, electrolysis, oxygen evolution, redox, scaling relations, seawater, transition metals

Received: December 12, 1912

Revised: December 12, 1912

Published online:

[1] W. K. Michener, E. R. Blood, K. L. Bildstein, M. M. Brinson, L. R. Gardner, *Ecol. Appl.* **1997**, *7*, 770.

- [2] M. S. Blondes, M. D. Merrill, S. T. Anderson, C. A. DeVera, Carbon dioxide mineralization feasibility in the United States. **2019**. <https://doi.org/10.3133/sir20185079>.
- [3] L. Plante, E. C. D. A. Simonetti, J. Wang, A. Al-Turki, X. Chen, D. Jassby, G. N. Sant, *ACS Sustainable Chem. Eng.* **2021**, 9, 1073.
- [4] C. J. Vörösmarty, P. B. McIntyre, M. O. Gessner, D. Dudgeon, A. Prusevich, P. Green, S. Glidden, S. E. Bunn, C. A. Sullivan, C. R. Liermann, P. M. Davies, *Nature* **2010**, 467, 555.
- [5] W. Tong, M. Forster, F. Dionigi, S. Dresp, R. Sadeghi Erami, P. Strasser, A. J. Cowan, P. Farràs, *Nat. Energy* **2020**, 5, 367.
- [6] S. Khatun, H. Hirani, P. Roy, *J. Mater. Chem. A* **2021**, 9, 74.
- [7] S. Trasatti, *Electrochim. Acta* **1984**, 29, 1503.
- [8] H. A. Hansen, I. C. Man, F. Studt, F. Abild-Pedersen, T. Bligaard, J. Rossmeisl, *Phys. Chem. Chem. Phys.* **2009**, 12, 283.
- [9] V. Sumaria, D. Krishnamurthy, V. Viswanathan, *ACS Catal.* **2018**, 8, 9034.
- [10] A. S. Dobrota, I. A. Pašti, S. V. Mentus, N. V. Skorodumova, *Phys. Chem. Chem. Phys.* **2016**, 18, 6580.
- [11] H. Ke, C. D. Taylor, *J. Electrochem. Soc.* **2020**, 167, 111502.
- [12] F. Dionigi, T. Reier, Z. Pawolek, M. Gliech, P. Strasser, *ChemSusChem* **2016**, 9, 962.
- [13] S. Dresp, F. Dionigi, M. Klingenhof, P. Strasser, *ACS Energy Lett.* **2019**, 4, 933.
- [14] J. G. Vos, T. A. Wezendonk, A. W. Jeremiasse, M. T. M. Koper, *J. Am. Chem. Soc.* **2018**, 140, 10270.
- [15] K. Izumiya, E. Akiyama, H. Habazaki, N. Kumagai, A. Kawashima, K. Hashimoto, *Mater. Trans., JIM* **1997**, 38, 899.
- [16] L. Yu, L. Wu, B. McElhenny, S. Song, D. Luo, F. Zhang, Y. Yu, S. Chen, Z. Ren, *Energy Environ. Sci.* **2020**, 13, 3439.
- [17] V. Petrykin, Z. Bastl, J. Franc, K. Macounova, M. Makarova, S. Mukerjee, N. Ramaswamy, I. Spirova, P. Krtil, *J. Phys. Chem. C* **2009**, 113, 21657.
- [18] V. Petrykin, K. Macounova, O. A. Shlyakhtin, P. Krtil, *Angew. Chem., Int. Ed.* **2010**, 49, 4813.
- [19] V. Petrykin, K. Macounová, M. Okube, S. Mukerjee, P. Krtil, *Catal. Today* **2013**, 202, 63.
- [20] P. Gayen, S. Saha, V. Ramani, *ACS Appl. Energy Mater.* **2020**, 3, 3978.
- [21] R. B. Wexler, G. S. Gautam, E. B. Stechel, E. A. Carter, *J. Am. Chem. Soc.* **2021**, 143, 13212.
- [22] G. Kresse, J. Hafner, *Phys. Rev. B* **1993**, 47, 558.
- [23] G. Kresse, J. Furthmüller, *Phys. Rev. B* **1996**, 54, 11169.
- [24] J. P. Perdew, K. Burke, M. Ernzerhof, *Phys. Rev. Lett.* **1996**, 77, 3865.
- [25] J. Sun, A. Ruzsinszky, J. P. Perdew, *Phys. Rev. Lett.* **2015**, 115, 036402.
- [26] S. Grimme, *J. Comput. Chem.* **2006**, 27, 1787.
- [27] S. Grimme, J. Antony, S. Ehrlich, H. Krieg, *J. Chem. Phys.* **2010**, 132, 154104.
- [28] S. Grimme, S. Ehrlich, L. Goerigk, *J. Comput. Chem.* **2011**, 32, 1456.
- [29] A. D. Becke, E. R. Johnson, *J. Chem. Phys.* **2005**, 123, 154101.
- [30] E. R. Johnson, A. D. Becke, *J. Chem. Phys.* **2005**, 123, 024101.
- [31] E. R. Johnson, A. D. Becke, *J. Chem. Phys.* **2006**, 124, 174104.
- [32] H. Peng, Z.-H. Yang, J. P. Perdew, J. Sun, *Phys. Rev. X* **2016**, 6, 041005.
- [33] A. Jain, S. P. Ong, G. Hautier, W. Chen, W. D. Richards, S. Dacek, S. Cholia, D. Gunter, D. Skinner, G. Ceder, K. A. Persson, *APL Mater.* **2013**, 1, 011002.
- [34] M. Methfessel, A. T. Paxton, *Phys. Rev. B* **1989**, 40, 3616.
- [35] J. Neugebauer, M. Scheffler, *Phys. Rev. B* **1992**, 46, 16067.
- [36] R. M. Bullock, J. G. Chen, L. Gagliardi, P. J. Chirik, O. K. Farha, C. H. Hendon, C. W. Jones, J. A. Keith, J. Klosin, S. D. Minter, R. H. Morris, A. T. Radosevich, T. B. Rauchfuss, N. A. Strotman, A. Vojvodic, T. R. Ward, J. Y. Yang, Y. Surendranath, *Science* **2020**, 369, 3183.
- [37] R. Tran, Z. Xu, B. Radhakrishnan, D. Winston, W. Sun, K. A. Persson, S. P. Ong, *Sci. Data* **2016**, 3, 160080.
- [38] S. P. Ong, W. D. Richards, A. Jain, G. Hautier, M. Kocher, S. Cholia, D. Gunter, V. L. Chevrier, K. A. Persson, G. Ceder, *Comput. Mater. Sci.* **2013**, 68, 314.
- [39] F. Pedregosa, G. Varoquaux, A. Gramfort, V. Michel, B. Thirion, O. Grisel, M. Blondel, P. Prettenhofer, R. Weiss, V. Dubourg, J. Vanderplas, A. Passos, D. Cournapeau, M. Brucher, M. Perrot, É. Duchesnay, *J. Mach. Learn. Res.* **2011**, 12, 2825.
- [40] J. Wellendorff, T. L. Silbaugh, D. Garcia-Pintos, J. K. Nørskov, T. Bligaard, F. Studt, C. T. Campbell, *Surf. Sci.* **2015**, 640, 36.
- [41] B. Hammer, J. K. Nørskov, *Nature* **1995**, 376, 238.
- [42] J. Rumble, *CRC Handbook of Chemistry and Physics*, CRC Press, New York, **2021**.
- [43] R. G. Pearson, *Inorg. Chem.* **1991**, 30, 2856.
- [44] F. Abild-Pedersen, J. Greeley, F. Studt, J. Rossmeisl, T. R. Munter, P. G. Moses, E. Skúlason, T. Bligaard, J. K. Nørskov, *Phys. Rev. Lett.* **2007**, 99, 016105.
- [45] P. W. Anderson, *Phys. Rev.* **1961**, 124, 41.
- [46] D. M. News, *Phys. Rev.* **1969**, 178, 1123.
- [47] B. I. Lundqvist, O. Gunnarsson, H. Hjelmberg, J. K. Nørskov, *Surf. Sci.* **1979**, 89, 196.
- [48] A. Nilsson, L. G. M. Pettersson, B. Hammer, T. Bligaard, C. H. Christensen, J. K. Nørskov, *Catal. Lett.* **2005**, 100, 111.
- [49] J. K. Nørskov, F. Abild-Pedersen, F. Studt, T. Bligaard, *Proc. Natl. Acad. Sci. USA* **2011**, 108, 937.
- [50] S. Zha, Z.-J. Zhao, S. Chen, S. Liu, T. Liu, F. Studt, J. Gong, *CCS Chem.* **2020**, 2, 262.
- [51] A. Kramida, Y. Ralchenko, J. Reader, NIST ASD Team **2021**. *NIST Atomic Spectra Database (version 5.9)*, [Online]. Available: <https://physics.nist.gov/asd>. National Institute of Standards and Technology, Gaithersburg, MD.
- [52] M. T. Greiner, L. Chai, M. G. Helander, W.-M. Tang, Z.-H. Lu, *Adv. Funct. Mater.* **2012**, 22, 4557.